

Revision : 1.8 Date : 2001/07/23 19 : 31 : 54

Advanced Exposure-Time Calculations: Undersampling, Dithering, Cosmic Rays, Astrometry, and Ellipticities

Gary Bernstein

Dept. of Astronomy, University of Michigan, 830 Dennison Bldg, Ann Arbor, MI 48109

`garyb@astro.lsa.umich.edu`

ABSTRACT

The familiar tools of Fourier analysis and Fisher matrices are applied to derive the uncertainties on photometric, astrometric, and weak-lensing measurements of stars and galaxies in real astronomical images. Many effects or functions that are ignored in basic exposure-time calculators can be included in this framework: pixels of size comparable to the stellar image; undersampled and dithered exposures; cosmic-ray hits; intrapixel sensitivity variations; positional and ellipticity errors as well as photometric errors. I present a formalism and a C++ implementation of these methods. As examples of their use, I answer some commonly arising questions about imaging strategies: What amount of dithering is ideal? What pixel size optimizes the productivity of a camera? Which is more efficient—space-based or ground-based observing?

Subject headings: methods: data analysis—space vehicles: instruments

1. Introduction

A basic exercise in the design of any astronomical camera or observing program is the estimation of the expected uncertainties, typically in the form of the photometric S/N ratio for a source of a given angular size in a given exposure time. Calculation of the S/N from aperture photometry is straightforward once the characteristics of the source, sky background, telescope, and detector have been ascertained. Derivations of these calculations, and web-based forms to perform them, can be found, for example, in the online documentation for the *HST* and for NOAO telescopes.

The common aperture-photometry formulae give a good rough estimate of the expected performance, but do not address several issues that are critical to optimizing a telescope design or observing-program design. The goal of this paper is to demonstrate a means to incorporate the following issues into an exposure-time analysis:

- Aperture photometry is not optimal; for unresolved sources, point-spread-function (PSF) fitting techniques are optimal. What is the accuracy of PSF-fitting photometry, especially for diffraction-limited point-spread functions (PSFs) from obscured circular apertures?
- The aperture formulae assume pixels either much smaller than or much larger than the optical PSF. The intermediate case is more common, and must be handled by creating an “effective PSF” which includes the pixelization.
- What are the errors for positional measurements on point sources (astrometry), galaxy magnitudes/colors (photometric redshifts), and galaxy ellipticities (weak lensing) under optimal analyses?
- How does undersampling or sub-pixel dithering affect accuracy?
- How do intrapixel sensitivity variations—*e.g.* the “picture frame” effect typical of HgCdTe detector pixels—affect these measurements? Likewise, what about charge diffusion within the detector?
- How does one quantitatively assess the impact of cosmic-ray hits without having to produce Monte-Carlo images?
- How does uncertainty in the source position affect photometric estimates?

The impetus for this work is to predict precisely the performance of various configurations of the proposed *Supernova Acceleration Probe*¹ (*SNAP*) satellite in its primary mission of supernova photometry, and its additional capabilities for weak lensing, photometric redshift, and astrometric surveys. In any astronomical camera design there is a trade-off in choosing an angular scale for the pixels: pixels small enough to finely sample the instrument resolution will prevent the degradation or aliasing of small-scale image information. Larger pixels, however, ameliorate read noise and may allow a larger field of view (FOV) in cases where detector pixels or bandwidth are scarce, or due to optics constraints. How severe is the penalty in photometric accuracy that one incurs from degraded sampling and resolution of larger pixels, and when does the loss outweigh the potential gains in FOV? Such tradeoffs are apparent in the 0!1 pixel scale of the WFPC2 wide-field CCDs. Given the volume of data taken with WFPC2, surprisingly few examinations of this tradeoff have been published. Several recent publications in the astronomical literature have discussed aspects of the more general exposure-time issues delineated above:

- Lauer (1999a)[L99a] gives a good review of the mathematics of undersampled images, and presents a method for removing aliased signals given an arbitrary pattern of dithered exposures. I will follow the L99a conventions where possible.

¹<http://snap.lbl.gov>

- Lauer (1999b)[L99b] continues with a discussion of point-source photometry in undersampled images, giving numerical results for the errors inherent in naive aperture photometry (and centroiding) on *HST* images. In this document I discuss extensively what L99b briefly mentions: that proper PSF-fitting photometry can be much more accurate, both for flux and centroid, than simple aperture-summing.
- Anderson & King (2000) give a lengthy discussion of the derivation of accurate astrometric information from WFPC2. The PSF-fitting techniques I use here would extract the same information from the images.
- Hook & Fruchter (2000) (and references therein) discuss the reconstruction of dithered undersampled images, particularly the DRIZZLE algorithm, which is a robust spatial-domain technique. In this document I will be concerned not with image reconstruction, but with quantitative extraction of various image moments (fluxes, centroids, and ellipticities), so I'll not make use of DRIZZLE.
- Kaiser, Tonry, & Luppino (2000) describe several kinds of PSF figures of merit with regard to the *WFHRI* concept of an array of ground-based tip-tilt telescopes. Further information may be found on the web pages for the *WFHRI* and *POI* projects.
- Technical reports for space-based telescope projects have addressed some of these issues, primarily with simulated data, *e.g.* Stiavelli, Hanley, & Robberto (1999) investigate the undersampling issue for *WFC3*, Rauscher, Isaacs, & Long (2000) examine the maximum cosmic-ray load for *NGST* instruments, and Petro & Stockman (2000) use the *NGST Mission Simulator*² to investigate optimal pixel sizes.

All of the techniques used in this paper are familiar to the image-analysis community and many of the elements are discussed in the above and other references. But I have not found in the astronomical literature: an application of the Fisher information matrix to point-source photometry in the presence of cosmic rays; a quantitative discussion of the effects of pixel size on weak lensing measurements; or a quantitative derivation of the required amount of dithering. More importantly, there is not to my knowledge a publication or software tool which combines all of these important effects to make detailed exposure-time estimates. That is the goal of this publication.

Following this Introduction is a general discussion of pixelization and sampling upon imaging observations, giving the analytical framework for the calculations. The next section briefly describes the implementation of these ideas in the ETC++ software package. §4 demonstrates the capabilities of the methods and software by providing quantitative answers to some general questions: what is the *S/N* penalty for oversized pixels? What amount of dithering is required to reach optimal *S/N*? Then I address some more specific questions about optimizing camera configurations, and comparing the performance of state-of-the art space-based imaging vs ground-based imaging.

²<http://www.ngst.stsci.edu/nms/main>

2. Pixelization, Sampling, and Noise

2.1. Fourier Description

Following the L99a and L99b exposition: The scene being imaged has intrinsic intensity distribution $O(x, y)$, with Fourier transform $\tilde{O}(k_x, k_y)$. The Fourier transform convention is “System 2” of Bracewell (1978):

$$O(\mathbf{x}) = (2\pi)^{-2} \int d^2k \tilde{O}(\mathbf{k}) e^{-i\mathbf{k}\cdot\mathbf{x}} \quad (1)$$

$$\tilde{O}(\mathbf{k}) = \int d^2x O(\mathbf{x}) e^{i\mathbf{k}\cdot\mathbf{x}}. \quad (2)$$

The telescope optics convolve the image with some optical point-spread function (PSF) $P(x, y)$ (which I take to have unit integral). With the above convention for the Fourier transform, the convolution $O * P$ has transform $\tilde{O} \cdot \tilde{P}$.

The pixelization of the image by the detector entails two operations: first, the optical image is convolved with the **pixel response function** (PRF) $R(x, y)$ (which I normalize to unit integral), and sampled on the two-dimensional grid of pixel centers on spacing a . The data from a single array readout are thus the image

$$I(x, y) = [O(x, y) * P(x, y) * R(x, y)] \text{III}\left(\frac{x}{a}, \frac{y}{a}\right) \quad (3)$$

where III is the 2d *shah* function,

$$\text{III}(u, v) \equiv \sum_{i=-\infty}^{+\infty} \sum_{j=-\infty}^{+\infty} \delta(u - i) \delta(v - j). \quad (4)$$

In the Fourier domain, the pixelated, sampled image is

$$\tilde{I}(\mathbf{k}) = [\tilde{O}(\mathbf{k}) \tilde{P}(\mathbf{k}) \tilde{R}(\mathbf{k})] * a\text{III}\left(\frac{ak_x}{2\pi}, \frac{ak_y}{2\pi}\right) \quad (5)$$

$$= \sum_{m=-\infty}^{\infty} \sum_{n=-\infty}^{\infty} \tilde{O} \tilde{P} \tilde{R}(k_x + m\Delta k, k_y + n\Delta k) \quad (6)$$

$$\Delta k \equiv \frac{2\pi}{a}. \quad (7)$$

The detected image, therefore, looks like the source image as convolved with an *effective PSF* (ePSF) $P' \equiv P * R$, and sampled at interval a . The sampling mixes power at spatial frequency $k_x + m\Delta k$ down to frequency k_x , leaving the nature of the original $\tilde{O}(\mathbf{k})$ ambiguous. This *aliasing* is detrimental to our efforts, as we cannot from a single measurement know exactly either the ePSF (from observing point-source stars) or the intrinsic scene O .

An optical telescope cannot transmit spatial frequencies beyond $\pm k_{\max} = \pm 2\pi D/\lambda$, where D is the largest dimension of the telescope aperture and λ is the wavelength. There is no aliasing if

$$\Delta k \geq 2k_{\max} \Rightarrow a \leq \lambda/2D. \quad (8)$$

For $D = 2$ meters, $\lambda = 1 \mu\text{m}$, this *Nyquist* sampling corresponds to $0''.05$ pixels.

When the data have been sampled at Nyquist or higher density, we can produce shifted, rotated, or deconvolved versions of the image with no ambiguity (apart from noise). In the *SNAP* mission, this will mean that subtraction of the host galaxy from supernova images will be essentially perfect, as long as the template image is Nyquist-sampled. This holds for other time-domain signals, such as microlensing, planetary transits, and Kuiper Belt surveys. For weak lensing surveys, it means that the systematic ellipticities imposed on galaxies by the PSF can, in theory, be removed nearly perfectly. Nyquist sampling is thus highly desirable.

2.2. Dithering

By taking a series of exposures with pointings *dithered* by a fractional pixel amounts, we can sample the ePSF-convolved scene more densely than the pixel grid.

It is important to realize that the two effects of pixelization are in fact separable: the ePSF depends on the size of the pixel through the PRF $R(x, y)$; but *the sampling density can be denser than the pixel grid a* . If we choose dither positions on a grid a/N , then we eliminate aliasing as long as $k_{\max} < N\pi/a$. We can therefore obtain Nyquist-sampled data even with large pixels. To first order this comes with no noise penalty: if we replace a single exposure of time T with a dithered grid of N^2 exposures each of time T/N^2 , then the total counts from the source are the same; the final image has the same number of sky photons per unit area (fewer per sample, but more samples per unit area). There is, however, an increase in overhead and read noise from the extra exposures, and the data rate must be higher.

What is the optimal dither pattern? L99a demonstrates that, for image reconstruction, a regularly interlaced grid offers the lowest noise. I have not encountered any reason to execute any other pattern. Interlacing makes the analysis straightforward, and the L99a and DRIZZLE techniques can be rendered equivalent in this case.

Given that interlacing can recover Nyquist sampling, the remaining drawback to larger pixels is the poorer resolution in the ePSF, which degrades the S/N for background-limited photometry and for centroid and ellipticity measurements of marginally resolved galaxies. I will quantify this below.

2.3. Space vs Ground

There are two important differences between space-based and ground-based data—one obvious and one more subtle—that suggest that a spaced-based observatory is likely to make use of larger pixels (relative to the PSF FWHM) than a ground-based imager:

1. **Dithering does not work easily for ground-based images.** This is because atmospheric seeing is constantly changing the PSF. Each successive exposure would be sampling a different PSF, rendering the de-aliasing difficult or impossible. If the PSF varies on spatial scales of $\Delta\theta$, then there must be enough PSF-template stars in each $\Delta\theta^2$ area to sample different pixel phases and solve for the unaliased PSF. Space observatories, however, can have exceptionally stable PSFs, longer than the time required to complete a dither sequence. For *HST*, the PSF varies significantly on the 90-minute orbit time due to thermal cycling. *SNAP* will rarely go into Earth eclipse, and even the Earthshine thermal load will vary only on the 15-day orbital period.
2. **The “dynamic range” of a ground-based PSF is larger than in space.** Colloquially an image is considered “Nyquist-sampled” if there are $\gtrsim 2$ pixels across the FWHM of the PSF. On large (8-meter) ground-based telescopes in excellent seeing, this requires pixels $\lesssim 0''.2$, which is easily accommodated, in fact difficult to avoid given the plate scales of 8m telescopes. In fact the PSF can have structure all the way to $\lambda/2D$, which is only 6 mas for V-band observations, so a formally complete sampling of the PSF is not practical. The high- k image power is strongly suppressed by the atmospheric seeing, however, so there is some sampling density at which the aliased power can be deemed insignificant. For a PSF generated by Kolmogorov turbulence ($\bar{P} = \exp[-(k/k_0)^{5/3}]$), sampling at 2.5 pixels per FWHM limits the aliased Fourier amplitude to about 1% of the total amplitude. This may not suffice for some applications, such as high-precision difference imaging, or weak-lensing surveys which need systematic ellipticity errors reduced to $\sim 10^{-4}$. Cutting the aliased amplitudes down to 0.1% requires 3.1 samples per FWHM.

A diffraction-limited circular telescope, on the other hand, has a FWHM of $\approx 1.0\lambda/D$ and can have no structure shorter than $0.5\lambda/D$. Hence putting ≈ 2 pixels (or samples) across the FWHM leaves *no* ambiguities.

The strict cutoff of the Airy PSF at $k = 2D/\lambda$ also means that space-borne observatories will be relatively insensitive to pixel response functions that depart from the ideal unit-square model. If the PRF has fine structure, it will be irrelevant, since the PSF does not pass spatial frequencies much smaller than the FWHM, which will be close to the pixel size. Similarly, subtle pixel-to-pixel variations in the PRF will not matter if they occur at high spatial frequencies.

All space-based observations intended for use as image-differencing templates or weak-lensing measurements should be interlaced by a factor N sufficient to reach Nyquist sampling. It is *not* necessary to Nyquist-sample exposure sequences intended solely for photometry of time-variable point sources, as investigated below.

2.4. Fisher Information for Point-Source Photometry

The most accurate method for point-source photometry is PSF-fitting. The vector of unknown parameters $\mathbf{p} = \{f, x_0, y_0\}$ (fluence and position) is varied to minimize deviations from a model PSF. We minimize

$$\chi^2 = \sum_i \frac{[\hat{I}(\mathbf{x}_i) - fP'(\mathbf{x}_i - \mathbf{x}_0)]^2}{\text{Var}(\hat{I}(\mathbf{x}_i))}. \quad (9)$$

Where \hat{I} is the measured fluence (counts per readout) at position \mathbf{x}_i and P' is the ePSF. It is straightforward to show that the covariance matrix of the fitted parameters is the inverse of the *Fisher information matrix* F :

$$F_{ij} = \sum_{\text{pixels}} \frac{\frac{\partial(fP')}{\partial p_i} \frac{\partial(fP')}{\partial p_j}}{\text{Var}(\hat{I}(\mathbf{x}_i))}. \quad (10)$$

If the centroid is known *a priori*, then the uncertainty in fluence is just $\text{Var}(f) = (F_{ff})^{-1}$. To calculate the Fisher matrix, we need the ePSF, the incident flux, and a noise model. The sum runs over all pixels in all exposures of a sequence. I will describe an observing sequence by the interlacing factor N , and by the number M of exposures taken at each of the N^2 dither positions. In *HST* parlance, M is the “CR-split.”

Ideally the noise is dominated by shot noise from the source and from a uniform sky background of n counts per unit solid angle per readout. In this case $\text{Var}(\hat{I}) = fP' + na^2$. In the limit of bright sources, the flux uncertainty reduces to $\text{Var}(f)/f^2 = (fMN^2)^{-1} = N_*^{-1}$, (N_* is total source counts), independent of the pixel or dithering configuration.

In the background-dominated limit, when we take the centroid as fixed, the flux uncertainty simplifies to

$$(S/N)^{-2} = \frac{\text{Var}(f)}{f^2} = \frac{na^2}{f^2 \sum [P'(\mathbf{x}_i)]^2}. \quad (11)$$

If the image has been sampled at the Nyquist density or higher, then we can apply Parseval’s Theorem to obtain the simple form

$$(S/N)^2 = \frac{N_*^2}{nNM^2 A_{SN}} \quad (12)$$

$$A_{SN} \equiv 4\pi^2 \int d^2k |\tilde{P}'(\mathbf{k})|^2 \quad (13)$$

$$= 4\pi^2 \int d^2k |\tilde{P}^2(\mathbf{k})| |\tilde{R}^2(\mathbf{k})|. \quad (14)$$

Thus in the limit of faint, Nyquist-sampled, unresolved sources, the S/N for detection/photometry depends up the effective area A_{SN} of the PSF, and we can easily see how the PRF affects this. The k -space integral form is particularly convenient since the Airy PSF is bounded to $k < 2D/\lambda$, and no convolutions must be executed.

Read noise and dark current produce white noise that can be subsumed into n in the simple formula (12). When the image is not Nyquist sampled, it is easier to transform the ePSF to x -space and use Equation (10).

The Fisher matrix also allows us to evaluate the astrometric accuracy for point sources. This is not a primary goal for *SNAP*, but I will present some results in §4.2.2. In the background-limited case, the one-dimensional uncertainty of point-source astrometry is simply quantified as

$$\sigma_x^2 = \frac{nNM^2 A_{\text{cent}}^2}{N_*^2} \quad (15)$$

$$A_{\text{cent}}^2 \equiv 4\pi^2 \int d^2k |k_x \tilde{P}'(\mathbf{k})|^2 \quad (16)$$

$$= 4\pi^2 \int d^2k k_x^2 |\tilde{P}^2(\mathbf{k})| |\tilde{R}^2(\mathbf{k})|. \quad (17)$$

2.5. Cosmic Rays

The incorporation of cosmic-ray (CR) hits into the Fisher formalism is easy. We just remove from the sum (10) the information contributed by pixels that are ruined. In the *SNAP* mission, we expect the CRs to span many pixels, while the ePSF will be $\lesssim 2$ pixels across. Hence the probability of losing the entire exposure’s information is essentially equal to the probability P_{CR} of the central pixel being contaminated during an exposure. For detectors with non-destructive readout (such as HgCdTe arrays), being sampled continuously during the exposure, the information lost is only that fraction accumulated *after* the CR hit.

There should be little difficulty identifying cosmic rays in space-borne images, as the vast majority of hits cover many pixels and deposit thousands of electrons. On the ground, cosmic rays cause negligible loss of information.

2.6. Galaxy Photometry

In the *SNAP* mission it will be important to derive accurate colors for resolved galaxies so as to obtain photometric redshift estimates for host galaxies. This places performance requirements on the S/N of galaxy photometry. For a galaxy with known intrinsic flux distribution $g(\mathbf{x})$, the best possible S/N on the total flux is derivable through the same Fisher information formalism as for point sources. This is equivalent to measuring the flux in a Wiener-filtered image. In practice, however, galaxies come in an infinite variety of shapes, so one cannot *a priori* choose the ideal filter for each image. More practical is to measure the flux through some predetermined aperture of shape $w(\mathbf{x})$:

$$f_w \equiv \int d^2x w(\mathbf{x})I(\mathbf{x}). \quad (18)$$

This weighted flux is not useful for studies requiring absolute total luminosities for galaxies, but will provide very accurate galaxy colors if matched apertures are used in different wavelength bands. I will assume, for simplicity, that both the galaxy and the weight are circularly symmetric. Then a simple propagation of errors gives a S/N ratio for the f_w , when Nyquist-sampled, of

$$\left(\frac{S}{N}\right)^{-2} = (2\pi)^2 \frac{\int d^2k \tilde{g} \tilde{P}' \tilde{w}^2 + n \int d^2k |\tilde{w}^2|}{\left[\int d^2k \tilde{g} \tilde{P}' \tilde{w}\right]^2}. \quad (19)$$

The first term in the numerator is the source shot noise, the second term is from the white-noise background arising from sky (or dark, read) counts of n per unit area.

A useful choice of weight is the Gaussian, $w = e^{-r^2/2\sigma^2}$. The Fourier transform is of course also a Gaussian, and Equation (19) can be evaluated for any candidate ePSF P' and galaxy profile $g(r)$. The size of the weight function σ can be adjusted to optimize the S/N for each galaxy on an image.

Clearly the effect of finite resolution in the PSF or PRF is to remove high- k information which might be present in the galaxy image. If the galaxy scale is larger than the PSF, then the PSF is irrelevant. Small galaxies reduce to the point-source limit.

Below I evaluate the resultant S/N for exponential-disk galaxies ($g \propto e^{-\alpha r}$). In this case a Gaussian-weighted flux measurement is only a few percent noisier than the optimally-weighted measurement.

2.7. Galaxy Ellipticities

For weak gravitational lensing measurements, we wish to detect small shears to the intrinsic shapes of galaxies. A poorly resolved or noisy galaxy image will inhibit this. It can be shown (Bernstein & Jarvis 2001, in prep.) that for a background-limited, nearly circular, Nyquist-sampled galaxy with radial flux profile g , the photon-noise contributions to the uncertainty in the ellipticity components e_1 and e_2 are each optimally

$$\sigma_e^2 = \frac{32\pi^2 n}{f^2} \left[\int d^2k \left| k \tilde{P}'(\mathbf{k}) \frac{\partial \tilde{g}}{\partial |k|} \right|^2 \right]^{-1}. \quad (20)$$

This is again easily calculated if we assume an exponential g and know our ePSF. In weak-lensing measurements, this photon noise level must be reduced below the *shape noise* level of $\sigma_e \approx 0.3$ attributable to the intrinsic variation in galaxy ellipticities. Non-circular galaxies will have slightly more photon noise than Equation (20) for a given magnitude and size, but this is a minor effect.

A further limitation to weak lensing measurements is systematic contamination of the intrinsic shapes by uncorrected artifacts of asymmetric ePSF's. As noted above, a Nyquist-sampled space-telescope image provides complete information on the ePSF, and hence will permit nearly-perfect

suppression of these systematic errors. Ground-based images must be sufficiently well-sampled to avoid aliasing any significant power. Furthermore, as the PSF is temporally and spatially variable in ground-based images, the mean spacing between bright PSF-template stars must be less than the angular scale of PSF variation. The space telescope has the luxury of constructing a PSF map by combining template stars from a series of exposures.

3. C++ Implementation

The above formulae have been implemented as a set of **C++** classes and driver programs. This **ETC++** software is available from the author. The interesting elements of the code are described here.

3.1. Classes

3.1.1. Psf

PSFs or ePSFs can be created as instances of the **Psf** class. A **Psf** can be an Airy pattern, a Gaussian, a square PRF, a Kolmogorov-turbulence seeing function, or an arbitrary convolution of any of these. Any **Psf** can return its value at some **k** vector, or the real-space transform; the point-source sensitivities A_{SN} and A_{cent}^2 can be calculated; or, given a **Galaxy** specification, the photometric accuracy Equation (19) or ellipticity variance Equation (20) can be calculated.

3.1.2. Galaxy

The **Galaxy** base class describes a galaxy image. A **Galaxy** has a flux and half-light radius. One can request the intensity of the galaxy at any point in x or k space, or the derivative $dg/d(\ln k)$ required for Equation (20). There are currently two options: **GalGaussian** and **GalExp**.

3.1.3. Params

The **Params** class contains all the specifications of an observatory and observing scheme that are necessary to calculate the S/N quantities: telescope aperture, obscuration, quantum efficiencies, filter specifications, detector characteristics, exposure times and sequences, cosmic-ray rates, etc. These are input from text files, and then can be parsed to produce the effective **Psf** for the observation, the source and sky count rates, etc.

3.1.4. Fisher Tools

Given an observing scheme, count rates, detector noise model, and ePSF, the `FisherCalc` class can produce the Fisher information matrix using Equation (10), then report the parameter errors. If cosmic rays are present, then there is a distribution of possible flux and centroid errors: this error distribution is calculated either by an exhaustive search of possible cosmic-ray outcomes, or by Monte-Carlo sampling of cosmic-ray outcomes. The uncertainty distribution can also include an integration over a grid of possible source positions relative to the pixel grid.

3.2. Executable Programs

There are top-level programs that make use of the above classes to return the photometric or astrometric S/N of point sources for a given observing scheme. Because the S/N depends upon pixel phase (for undersampled images) and cosmic-ray outcomes, the S/N levels are in fact reported as percentile values, *e.g.* the median, 5th and 95th percentile flux errors. Other top-level programs report the photometric and ellipticity measurement speeds for galaxies.

More interesting is the `optimize` program, which seeks the observing scheme (exposure times, interlacing and CR-split factors) that reaches a desired S/N on point sources in minimum total observing time. The target S/N must be specified, as well as the “confidence level” giving the fraction of sources which must be measured to the target accuracy. This calculation is meant to be quite realistic, including all time overheads, cosmic rays, sampling, etc.

4. Applications

This section demonstrates some applications of the above tools. Some of the questions addressed here are very general, while some are specific to the *SNAP* optimization.

4.1. How Much Dithering Is Required?

If the pixels are larger than the Nyquist size $0.5\lambda/D$, what interlacing factor N is required to recover most of the photometrically useful information? Estimation of the point-source flux via PSF-fitting does not require Nyquist sampling, as long as an unaliased PSF template is available; the loss of information from aliasing can be minor if the sampling is adequate.

Figure 1 shows the recovered S/N ratio for a diffraction-limited PSF observed on perfect square pixels of some size $P\lambda/D$, for various interlacing factors N . The total observing time is held fixed, I ignore overheads and read noise, and assume here a background-limited observation. The heavy line shows the S/N for Nyquist-sampled images (relative to infinitesimal pixels). The degradation

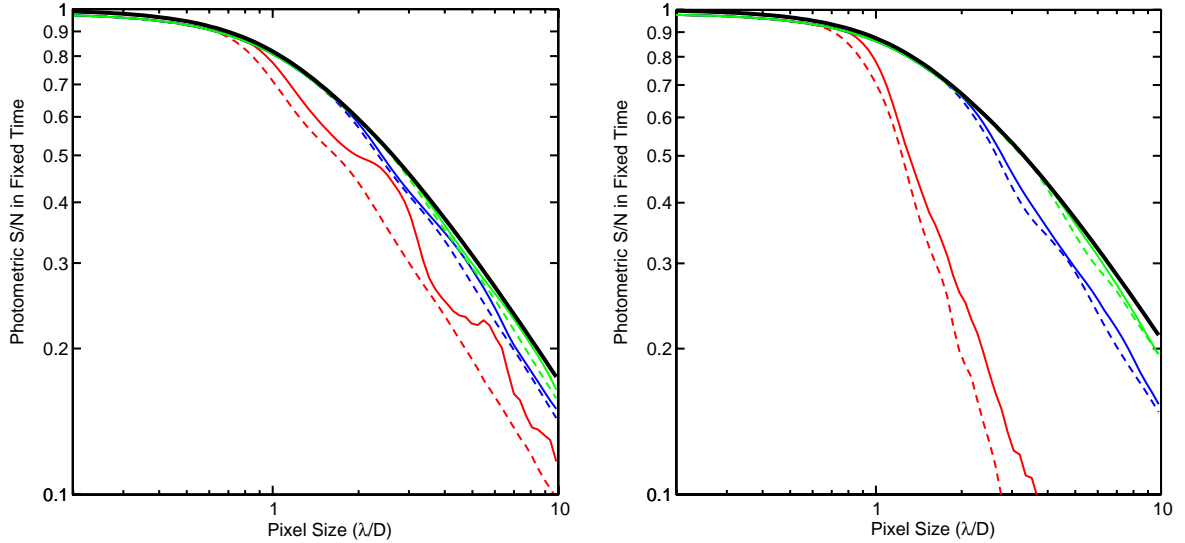


Fig. 1.— The S/N ratio attained in fixed integration time is plotted as a function of the pixel size (in units of λ/D) for the limiting case of background-limited, uncrowded point-source photometry with no readout overheads and a diffraction-limited optical PSF. In the left-hand panel, the pixel response function is a perfect square, but on the right-hand side the pixels are assumed to have a dead zone in the outer 10% of each edge. The heavy black line assumes that the image has been interlaced to reach Nyquist sampling. The solid red line is the median S/N when there is no interlacing at all; the S/N at the least favorable pixel phase is the dashed red line. The blue and green lines give the corresponding data for exposure interlacing factors of $N = 2$ and 3 , respectively. Interlacing by a factor 3 recovers nearly all the available S/N in every case.

of point-source S/N as the PRF broadens is apparent. The solid red line shows the median S/N in the $N = 1$ case, *i.e.* no interlacing. There is up to 30% degradation when $P > 1$. The dashed red line shows the S/N at the worst pixel phase.

A little dithering helps a lot, however. For $N = 2$ (blue lines), both the RMS and worst-case are very close to Nyquist for $P \lesssim 8$. For $N = 3$ (blue lines), both RMS and worst-case are within a few percent of Nyquist at all pixel sizes. Photometrically speaking, therefore, there is little point to interlacing at $N > 3$. The reason is that the PRF itself rolls off sufficiently quickly that there is little aliasing for $N > 3$, regardless of the PSF.

Many detectors do not have uniform response across the geometric pixel square. As a canonical example I consider a case where the pixel contains dead “gutters” at the outer 10% of each pixel edge, so the active area covers only 64% of the geometric pixel. For oversized pixels one might worry that the star could fall into the dead area. Since the PSF is not finite, there is always some flux in the sensitive areas. While naive aperture photometry will fail in this case, a PSF fit will recover an unbiased flux estimate and centroid—but the loss of information could be significant, as intuition suggests. The second panel of Figure 1 shows the photometric S/N vs pixel size in this case. Non-interlaced exposures ($N = 1$, red line) are far worse than Nyquist sampling for $P > 1$.

Interlacing with $N = 2$ recovers the Nyquist S/N up to $P \approx 2$, however, and $N = 3$ interlacing again recovers almost the full Nyquist S/N for any sensible pixel size.

Once the ePSF is known from bright stars, the non-uniformity of the PRF is immaterial. Of course if each pixel has a different PRF, then the template ePSFs will be incorrect, leading to magnitude errors. But it is important to recall that only variations at spatial frequencies below $2\pi D/\lambda$ can make any difference. Unless the PRF is grossly larger than the Airy disk (and the charge-diffusion scale), inter-pixel variations will be strongly damped in the ePSF.

I plot in Figure 2 the relative *position* accuracy for a pixellated Airy PSF as a function of pixel size and interlacing. The penalty for large pixels is more severe for astrometric observations than for photometry. Interlacing at $N = 2$ approaches Nyquist centroiding errors for $P \lesssim 2$ in all cases; likewise $N = 3$ recovers all information up to $P \lesssim 3$. For $P > 3$ we see that $N = 3$ interlacing recovers the Nyquist accuracy in the median case, but an unfavorably positioned star can have greatly degraded astrometric accuracy.

In contrast to the photometric measurement, an astrometric measurement of a bright star is degraded by large pixels. But the dependence of σ_x on P is not as steep as in the faint (background-limited) case.

For point-source measurements, therefore, I find it is typically necessary to interlace exposures only to about half the Nyquist density, though complications may arise for very large ($> 3\lambda/D$) pixels. If a large number of exposures must be taken, however—*e.g.* to avoid saturation or cosmic-ray loading—one might as well interlace to the Nyquist level.

4.2. Optimization of Pixel Scale

What choice of pixel scale allows a science goal to be achieved with the fewest resources? The most typical scarce resource is total observing time T . There may be an additional constraint on the FOV imposed by the optical design, in which case one typically tries to reduce the pixel scale P until read noise is important or $P \lesssim 0.5$. Less obvious is the optimal pixel scale P in cases where the number of pixels N_{pix} has an upper bound imposed by detector cost, telemetry bandwidth limitations, or engineering constraints.

4.2.1. Background-limited Point-Source Photometry

The tradeoffs are most easily understood for background-limited point-source photometry, in which case the detector geometry is fully described by the A_{SN} “PSF area” in Equation (12). Consider the PRF to be a square of angular size $P\lambda/D$. Figure 3 plots the value of A_{SN} as a function of P . In the limit $P \ll 1$ of fine sampling, A_{SN} reduces to that of the Airy pattern, $A_{\text{Airy}} = 3.35(\lambda/D)^2$ (for pupil obscuration $\epsilon = 0.25$). The sky noise is thus equivalent to that

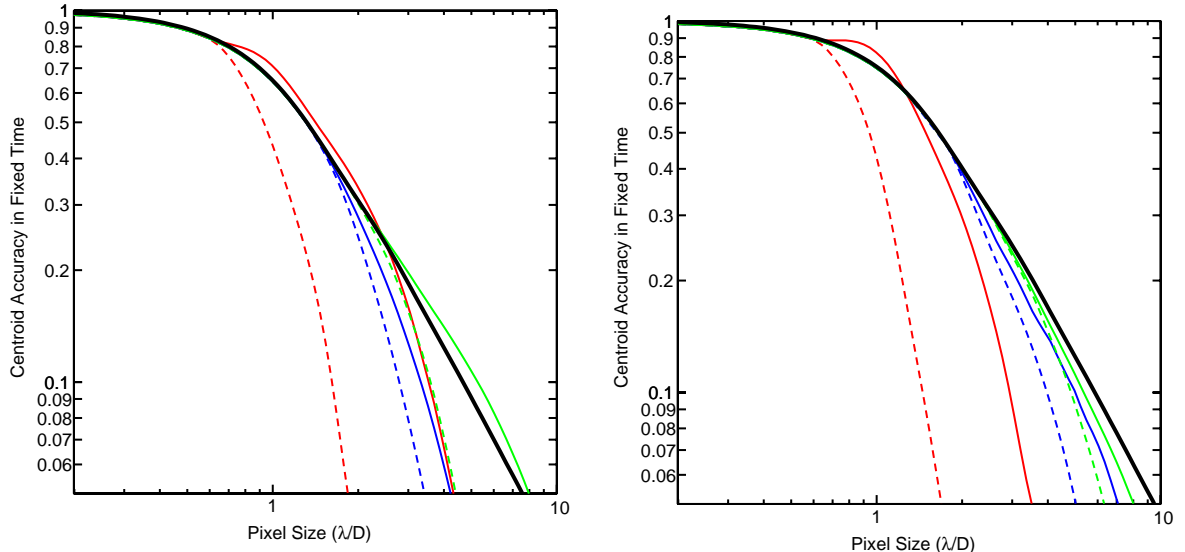


Fig. 2.— The accuracy of the centroid determination for a background-dominated point source in fixed observing time is plotted as a function of pixel size. As in Figure 1, the left-hand side is for an ideal square pixel and the right-hand side is for pixels with a 10% “gutter.” Line types are also as in Figure 1. The penalty for large pixels is more severe for astrometric observations than for photometry. For large pixels we see that $N = 3$ interlacing is, in the median case, nearly as good (or better!) than Nyquist interlacing, but if the star falls at an unfavorable pixel phase, the astrometric accuracy can be greatly degraded when $P \gtrsim 2$.

in a circular aperture of radius $1.03\lambda/D$. In the limit $P \gg 1$, A_{SN} is simply the pixel area $A_{pix} = P^2(\lambda/D)^2$. It should be noted, however, that the common heuristic approximation $A_{SN} \approx A_{Airy} + A_{pix}$ will *underestimate* the A_{SN} , and hence the required exposure time, by up to 40% between these limits. In particular, note that Nyquist-sampling pixels ($P = 0.5$) degrade the Airy A_{SN} level by 13%, while pixels at the Airy FWHM of $P = 1.22$ degrade the speed by about a factor 1.5, assuming interlacing to the Nyquist level.

The degradation of point-source S/N is more severe if the detector has significant diffusion of charge before collection into pixels. The dashed line in Figure 3 shows A_{SN} when there is Gaussian charge diffusion with σ of one-half pixel. In this case even the Nyquist-sized pixels increase A_{SN} by 30%, and the A_{SN} for $P = 1$ is ≈ 10 pixels, three times worse than the pure Airy value.

On the other hand, the overall speed of a photometry project can be an increasing function of pixel size if the number of pixels is constrained. If the science goals require surveying a fixed, large number of square degrees to a given depth, then the total time to complete the project scales as

$$T \propto \frac{A_{SN}}{N_{pix}P^2}. \quad (21)$$

So for fixed pixel count N_{pix} , the figure of merit is P^2/A_{SN} , which we see from Figure 3 is always increasing with P , to an asymptotic value of unity. A grossly undersampled camera at $P = 10$

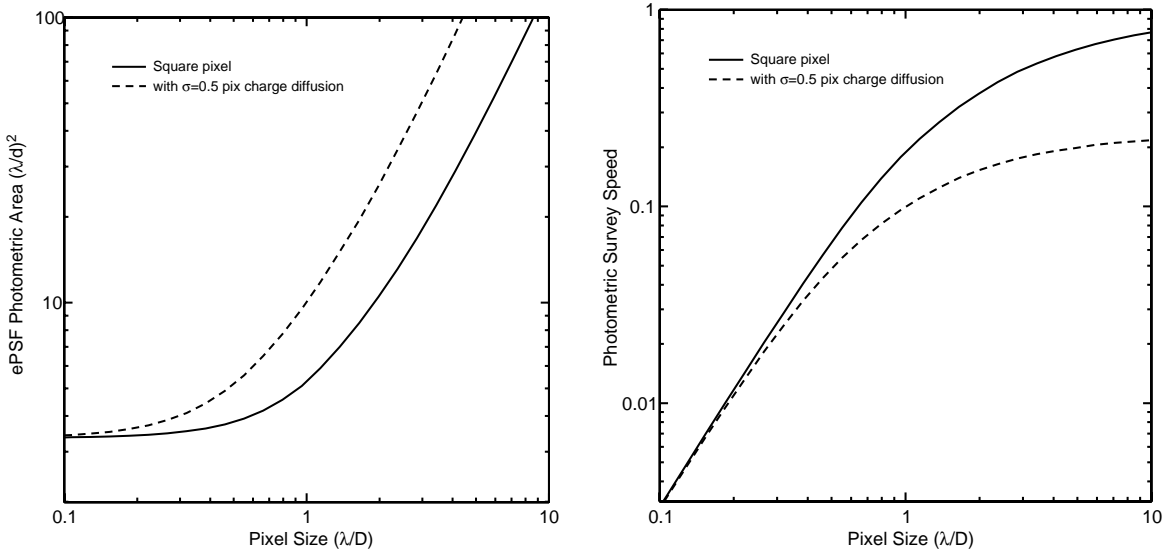


Fig. 3.— On the left plot, the effective area A_{SN} of the ePSF for background-limited point-source photometry is plotted vs pixel size. The solid line is for a perfect square pixel atop a diffraction-limited PSF from a telescope with 30% pupil obscuration. The dashed line shows the effect of charge diffusion with $\sigma = 0.5$ pixels. The time to complete an observation to fixed S/N will scale as this parameter. The penalty from charge diffusion is substantial. On the right side is the speed to survey a given sky area to a given S/N , assuming that the number of pixels is fixed. Larger pixels always help, as long as the FOV increases proportionately.

conducts a point-source survey 10 times faster than a Nyquist-sampled camera! In the presence of charge diffusion, the undersampled camera is still 4× faster.

For sources brighter than the sky background, the S/N is independent of pixel size, hence the survey speed grows with the FOV, or $\propto P^2$ if N_{pix} is fixed—an even stronger advantage than the background-limited case.

The gains of larger pixels are realized only as long as the FOV increases linearly with pixel size. In reality, aberrations and engineering difficulties will place lower bounds on the focal length and upper bounds on the FOV. But these results suggest a very strong motivation toward coarse pixels in space-based survey projects. Coarse pixels can have other well-known practical advantages with respect to dark current, read noise, and telemetry rates.

The above calculations assume PSF-fitting on isolated point sources. This is wholly appropriate for time-domain projects (supernova hunting, microlensing, moving objects) in which a high-S/N template image can remove all but the (rare) variable objects from an image. For other projects, however (crowded-field stellar photometry), the large pixels will impose a severe crowding penalty, and $P \lesssim 1$ will be strongly preferred. A project for which morphological information is essential will of course suffer with coarse pixels as the high-frequency information is strongly attenuated when $P \gg 1$. Such projects really require optimization of image reconstruction as discussed in

L99a and Hook & Fruchter (2000).

Even time-domain projects will suffer significantly when the pixels become large enough that the shot noise from neighboring (static) objects begins to outstrip the ecliptic sky background in a typical pixel. This occurs when the pixel size is comparable to the typical spacing between objects that have surface brightness above that of the zodiacal light background. At high galactic latitudes, stars are rare, and galaxies with surface brightness above 23–24 mag arcsec⁻² will be many arcseconds apart from each other. For nearby supernovae, the host galaxy’s central surface brightness may exceed the zodiacal light, so we favor small pixels which do not blend the nucleus/center with the supernova. Microlensing and stellar-variability surveys will typically point toward nearby galaxies with many bright individual stars, so very large pixels may increase the effective background level.

In summary, for survey-oriented projects there are very strong efficiency gains from $P \gtrsim 1$ if pixel count and/or telemetry bandwidth are limited.

4.2.2. Point-Source Astrometry

Astrometric measurements place a higher premium on compact ePSF than do flux measurements since the centroid is a higher moment (first) of the stellar image than is the flux (zeroth). In Figure 4 I plot the relative survey speed for a background-limited, Nyquist-sampled astrometric measurement as a function of pixel size, again assuming a fixed N_{pix} . In this case there is a very well-defined optimum size of $1 \lesssim P \lesssim 2$. Unlike the flux-measurement case, there are no gains to larger pixels; bright stars as well as background-limited stars will prefer intermediate pixel scales. The only reason to use Nyquist-sampled pixels ($P \leq 0.5$) on an orbiting astrometric satellite would be if there is no FOV gain from a coarser scale.

4.2.3. Galaxy Ellipticities

The optimization for weak-lensing observations depends upon the size of the target galaxy. Figure 5 shows the time required to reach $\sigma_e < 0.2$ for a background-limited galaxy as a function of the galaxy size r_h at fixed galaxy magnitude. When the galaxy is large, the required time scales as r_h^2 since the galaxy is well-resolved, but is spread over more background. When the galaxy size r_h is below the ePSF size, the required time grows as a strong function $\sim r_h^{-4}$ because the ellipticity information is suppressed by the ePSF. There is, hence, a significant penalty to making the pixel scale too coarse, even if the FOV can be increased along with pixel size.

This is quantified further in Figure 5, in which I plot the relative speed vs pixel size P for lensing measurements. If t is the time required to reach $\sigma_e < 0.2$, then the survey speed is $\propto N_{\text{pix}} P^2 / t$. The Figure plots relative lensing survey speeds as a function of pixel size under the assumption of fixed N_{pix} . In this case $\lambda/D = 0!1$, and the curves show the speed for exponential-disk galaxies

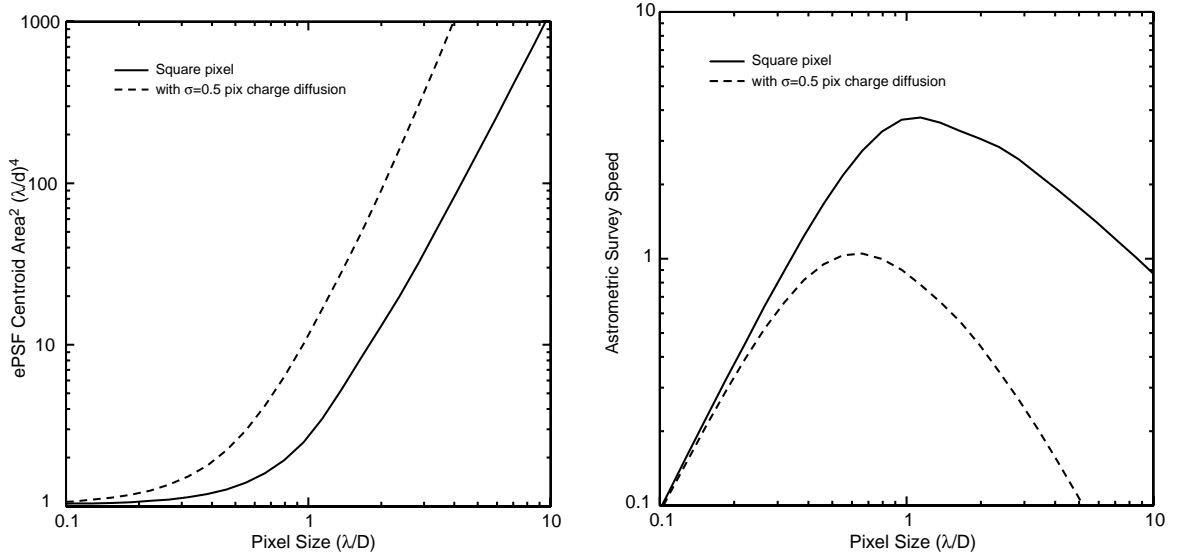


Fig. 4.— On the left plot, the effective area A_{cent}^2 of the ePSF for background-limited point-source *astrometry* is plotted vs pixel size. The solid line is for a perfect square pixel atop a diffraction-limited PSF from a telescope with 25% pupil obscuration. The dashed line shows the effect of charge diffusion with $\sigma = 0.5$ pixels. The time to obtain fixed astrometric accuracy on a single source scales as A_{cent}^2 . The penalties for large pixels and charge diffusion are more severe than for photometry (Figure 3). The right side plots the speed for an astrometric survey (sky coverage divided by time to obtain given centroid accuracy) vs pixel size, given a fixed pixel count. There is a clear optimum pixel scale at 1–2 λ/D .

with $0''.02 \leq r_h \leq 0''.8$. The vast majority of observable galaxies fall within this range (Gardner & Satyapal 2000; Roche *et al.* 1998). The smallest and largest galaxies are very poorly observed with this λ/D regardless of pixel size. For the intermediate sizes, we see that the optimal pixel scales are $1 \lesssim P \lesssim 4$. If N_{pix} is fixed, therefore, it is once again advisable to make the pixels $\gtrsim \lambda/D$ in size—not at the Nyquist size $0.5\lambda/D$.

4.3. Comparison of Ground-Based and Orbiting Observatories

Here I use the methods and software described above to compare the survey capabilities of two proposed observatories: *SNAP* would represent the state of the art in orbiting imaging observatories late in the decade, with a 1 deg^2 CCD FOV behind a 2-meter telescope. The *Large Synoptic Survey Telescope*³ (*LSST*) would likewise represent the state of the art in large ground-based survey telescopes, with $\approx 7 \text{ deg}^2$ FOV behind an 8.4-meter primary mirror. In terms of imaging throughput, each instrument would be ≈ 2 orders of magnitude faster than present-day counterparts. The space and ground observatories, however, have very distinct strengths, and would likely be focused

³<http://www.lsst.org>

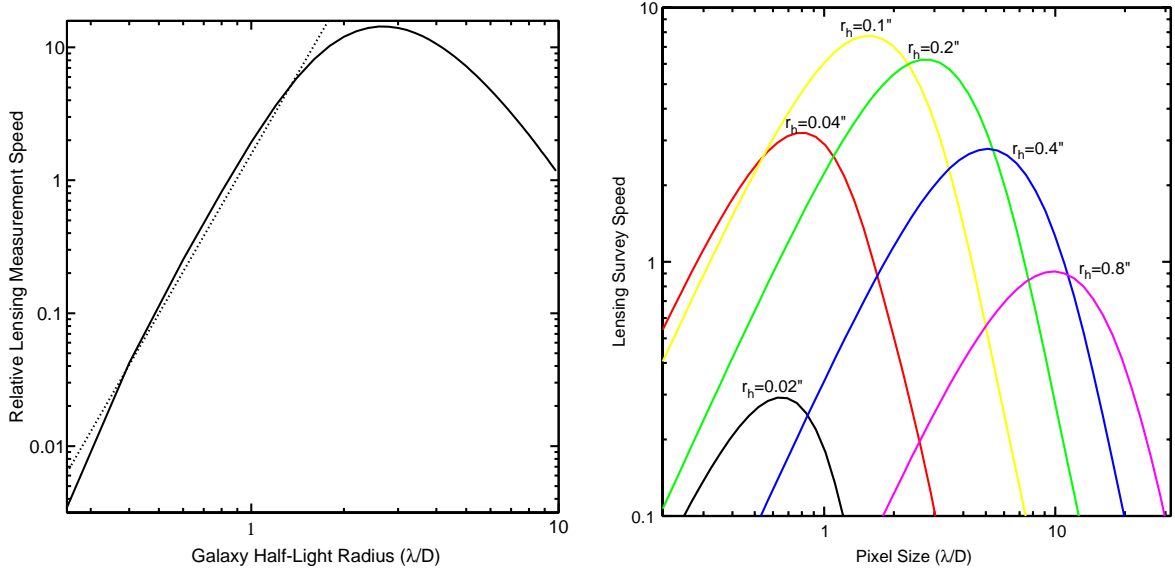


Fig. 5.— On the left-hand side, the speed for a weak-lensing survey (inverse of time to reach ellipticity accuracy of 0.2) is plotted versus the half-light radius r_h of an assumed exponential-disk galaxy of fixed magnitude. For this plot it is assumed that the pixels are of size $0.5\lambda/D$. Large galaxies are slowly measured due to sky noise. Poorly resolved galaxies are strongly penalized: the dotted line shows speed $\propto r_h^{-4}$. On the right-hand side, lensing-survey speed is plotted versus choice of pixel size, given a fixed pixel count and galaxies of a given r_h . All galaxies are given a common magnitude and are assumed to be background-limited. For this plot it is assumed that $\lambda/D = 0''.1$. Galaxies with $r_h < 0.4\lambda/D$ are poorly measured at any pixel size; for measurable galaxies, the optimum pixel sizes are in the range $0.8\text{--}3\lambda/D$. For galaxies that are many times larger than λ/D , grossly oversized pixels are favored if they come with increased FOV.

on very different science goals.

The assumed characteristics of the two observatories are detailed in Table 1. The important differences to note are:

- *SNAP* pixels are $0''.1$, corresponding to $2\lambda/D$ for the $1\text{ }\mu\text{m}$ diffraction-limited PSF, whereas the *LSST* pixels are $0''.25$ to sample the presumed $0''.5$ FWHM ground-based seeing.
- Dithering is assumed to be ineffective from *LSST* due to the time-variable PSF. An optimal interlacing factor is chosen for each proposed *SNAP* observation.
- *SNAP*, in high-earth orbit, is assumed to be on target nearly full time. For *LSST* I presume that on average only 30% of the time is useful after losses due to daylight, moonlight, and clouds.
- *LSST* has a somewhat larger pixel count, and is assumed to have faster readout (5s vs 20s).
- The *LSST* secondary obscuration is quite large (55% of the primary aperture) compared to *SNAP* and typical 2-mirror telescopes.

- The *SNAP* background is taken to be the zodiacal brightness at the North ecliptic pole, while the *LSST* sky is the new-moon Cerro Tololo zenith sky brightness. *LSST* zenith atmospheric extinction is taken to be that at Cerro Tololo as well.

For wavelengths beyond $1\text{ }\mu\text{m}$, I posit either *LSST* or *SNAP* to be equipped with a mosaic of 16 $2\text{k}\times 2\text{k}\times 15\mu\text{m}$ HgCdTe array detectors, with 4e read noise and 0.02 e/s dark current. The HgCdTe pixels are assumed to have a 10% dead zone on each edge. I presume for now that the NIR arrays would have the same focal ratio and cosmic-ray rates as the posited CCD arrays.

4.3.1. Point-Source Photometric Survey

Figure 6 compares the speed for a photometric point-source survey on *LSST* relative to *SNAP*. The figure of merit being compared is the number of square degrees of sky per 24-hour period which can be surveyed for given source magnitude. I demand that at least 95% of the sources at the chosen magnitude be measured with $S/N \geq 7$ (recall that cosmic rays and varying pixel phases make the S/N a random variable).

We can reach the following conclusions:

- When the sources have $AB < 27$ and are observable in B and V bands (*e.g.* a low-redshift supernova search), the ground-based search is more efficient by a factor of 2–5.
- For R -band observations, or for very faint B -band sources, there is no clear advantage.
- When the sources move to I band and $AB > 27$, the faint background and resolution of the space platform start to win. I -band surveys are 3–5 times faster from orbit.
- In Z -band the space advantage is 7–10 times.
- In the NIR the space advantage is of course huge due to background issues. In J , the 2m *SNAP* is 30–100 times faster than the 8.4m *LSST*, given a comparable investment in IR array detectors. The H band advantage is even larger.
- Also shown on the plot are the relative figures of merit for the proposed $8\text{k}\times 8\text{k}$ NIR/visible imager aboard the 8-meter *Next Generation Space Telescope* (NGST). In the NIR, the larger aperture makes NGST $\approx 2\times$ faster than *SNAP*, but only for the very faintest sources observable by *SNAP*. In I -band, the much larger FOV of *SNAP* makes the survey at least $3\times$ faster.

This of course is just a noise analysis; there are systematic-error and cost issues as well, the former favoring *SNAP* and the latter *LSST*. In particular, note that the above analysis has assumed isolated point sources—which is appropriate to a time-domain search with perfect difference

Table 1. Assumed Observatory Characteristics

Quantity	<i>SNAP</i> Value	<i>LSST</i> Value
Telescope Aperture	2.0 m	8.4 m
Focal Length	21.6 m	8.2 m
Fractional Diameter of Pupil Obscuration	20%	55%
Gaussian σ for Aberrations/Seeing	0'.05	0'.5
Optical Transmission	83% (Vis & NIR), 50% (UV)	70% of zenith atmosphere ¹
CCD Pixel Size	10.5 μm	10.5 μm
CCD Read Noise	4 e	4 e
CCD Quantum Efficiency	LBL CCD ²	LBL CCD ²
CCD Charge Diffusion Sigma	3.5 μm	3.5 μm
CCD Dark Current	0.0013 e s^{-1} pix $^{-1}$	0.0013 e s^{-1} pix $^{-1}$
CCD Readout Time	20 s	5 s
CCD Cosmic-Ray Rate	0.00013 s $^{-1}$ pix $^{-1}$	0
CCD FOV	1.0 deg 2	7.0 deg 2
NIR Pixel Size	18 μm	18 μm
NIR Read Noise	4 e	4 e
NIR Quantum Efficiency	HgCdTe ³	HgCdTe ³
NIR Charge Diffusion Sigma	5 μm	5 μm
NIR Dark Current	0.02 e s^{-1} pix $^{-1}$	0.02 e s^{-1} pix $^{-1}$
NIR Readout Time	1 s	1 s
NIR N_{pix}	6.4×10^7	6.4×10^7
Sky Brightness	Ecliptic Pole Zodiacial ⁴	CTIO Zenith Dark Sky ⁵
Duty Cycle	100%	30%

¹Atmospheric extinction from Hamuy *et al.* (1994,?)

²Expected QE for High-Resistivity CCD used, (Groom 2000)

³Measured QE for existing HgCdTe HAWAII arrays

⁴Zodiacial brightness from Leinert *et al.* (1997)

⁵CTIO zenith sky brightness from Massey *et al.* (2000)

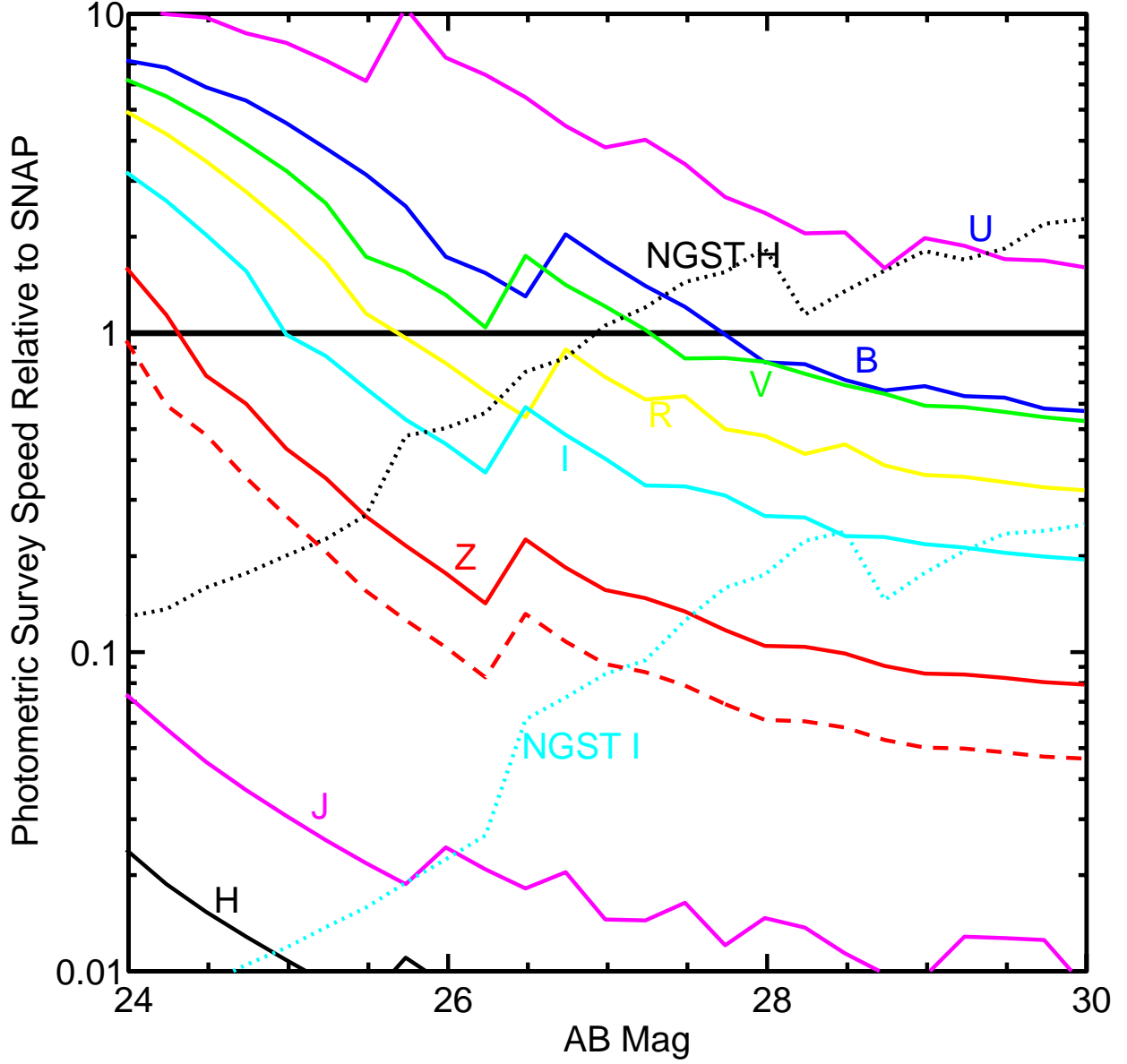


Fig. 6.— The survey speed for photometric observations (sky coverage divided by time to fixed S/N) is given for *LSST* relative to *SNAP*. Different filter bands are labeled. The dashed red curve shows the result of having $0.^{\prime\prime}7$ FWHM seeing instead of $0.^{\prime\prime}5$ (solid red) in *Z* band. Poorer seeing would shift all other wavebands similarly. Two curves are shown for the speed of an NGST NIR/visible 8k imager relative to *SNAP*. I demand in each case that 95% of point sources be measured to $S/N \geq 7$; the jumps in the curves occur where cosmic-ray hits become likely in > 5% of pixels.

imaging. For crowded-field photometry, however (color-magnitude diagrams for distant systems, Cepheid measurement, etc.), the space telescopes gain a large factor from better resolution.

Note also that both observatories' designs could be tweaked to improve performance on this measure, but the ultimate restrictions on FOV, telemetry rate, etc. require a full engineering analysis.

4.3.2. Photometric Redshifts

For lensing applications, pre-determination of supernova host-galaxy redshifts, and a slew of galaxy-evolution studies, photometric determination of galaxy redshifts will be of huge benefit. We thus need to know the speed at which we can measure colors of resolved objects to a nominal accuracy. I take here a target $S/N \geq 20$ for photo-z applications.

Figure 7 plots show the relative speeds of the nominal *SNAP* and *LSST* configurations for photometry of galaxies. Here it has been assumed that fluxes of galaxies are being measured through Gaussian apertures, and the aperture size has been selected to optimize the S/N. This is close to an optimal procedure for the exponential-disk galaxies considered here. Poisson noise from sky, source, and dark counts is included. Read noise is negligible. The plots are for $AB = 27$ mag galaxies of various sizes, but the relative speeds will apply to any source that is fainter than the background. Again an optimistic duty cycle of 30% has been assumed for the ground-based survey.

The relative speed is plotted as a function of galaxy half-light radius. The typical sizes for faint galaxies found in the HDF-South STIS images are marked with triangles (from Gardner & Satyapal (2000)). Galaxy photometry is seen to be faster from the ground in the blue, but a good deal faster from space for Z , J , and H -band observations, with a near tie in R and I bands. The black line shows the relative speed when all four visible bands B , R , I , & Z are to be done sequentially.

For nearby galaxies with sizes $\gtrsim 0''.5$, any CCD-based photometric redshift survey is better done from the ground. But the orbiting observatory wins heavily in the NIR bands, or for the smaller galaxies more typical at $m_{AB} \gtrsim 27$.

No flat-fielding errors or crowding have been included here. The latter will be important for ground-based images at 29–30 mag.

4.3.3. Ellipticity Measurements

Figure 8 shows the relative speeds for lensing observations. In each case, the figure of merit is the time it takes for the background noise to be reduced to the point where the galaxy ellipticity is measured to an accuracy of 0.2 or better. The galaxy is assumed here to have $m_{AB} = 27$, and

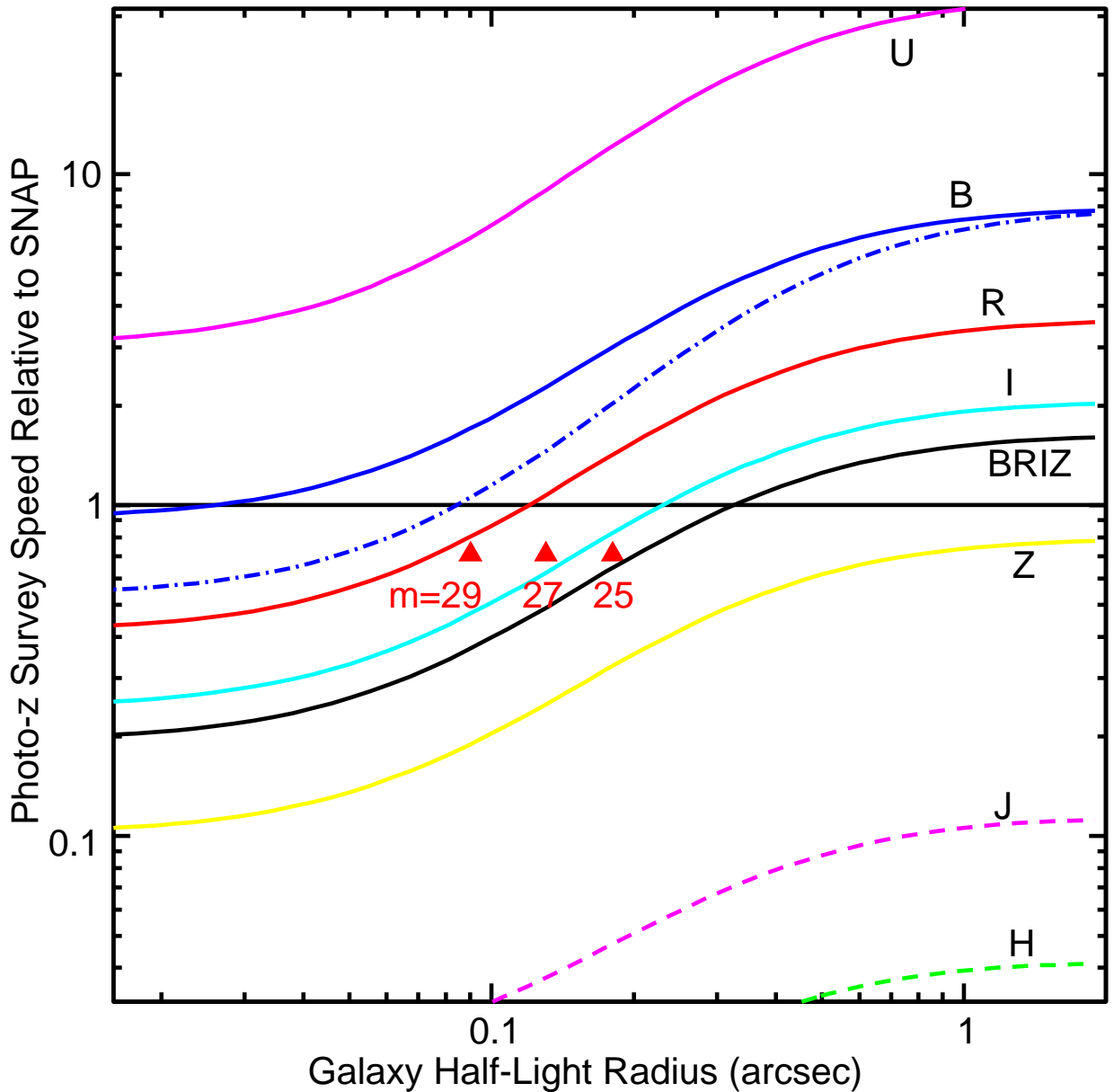


Fig. 7.— The survey speed for galaxy photometric redshift surveys (sky coverage divided by time to fixed flux error in Gaussian apertures) is given for *LSST* relative to *SNAP*, for various wavelengths. Typical faint-galaxy sizes are marked. The ground observations are favorable only for larger galaxies at bluer wavelengths, as expected.

be a circular exponential disk; the relative speeds will remain the same for any background-limited case. Overhead and cosmic-ray hits are ignored, as is appropriate for deep images.

A lensing survey can be conducted in the filter of choice (apart from a desire for photometric redshifts, described above). One would likely choose something like I -band for a space observation and R band from the ground to obtain the shape information most rapidly. From the figure it is clear that *LSST* surveys large galaxies about 4–5 times faster than *SNAP*, due to the larger aperture and FOV, if I assume fixed m_{AB} vs wavelength. In actuality most galaxies are redder than this, so the relative speed of *LSST* will be decreased by about $2\times$ (if $\langle R_{AB} - I_{AB} \rangle \approx 0.4$ mag).

For galaxies smaller than $0''.3$ half-light radius, *SNAP* is faster because the ground-based seeing dilutes the signal and squelches the ellipticity signal. Indeed the required exposure times rise very rapidly ($\propto r^{-4}$) when galaxies are poorly resolved, so in fact an orbiting observatory is essentially required to extract lensing information the bulk of galaxies at $m_{AB} \gtrsim 25$. High-order adaptive optics are never likely to cover sufficient FOV to make practical weak-lensing observations, but the wide-field tip-tilt-correction scheme of *WFHRI* (Kaiser, Tonry, & Luppino 2000) may allow ground-based weak-lensing observations of smaller galaxies. I hope to analyse the relative merits of the *WFHRI* configuration in the near future; my expectation (and that of Kaiser, Tonry, & Luppino (2000)) is that *WFHRI* will be faster for BVR observations but the low background of *SNAP* will win out in Z or I . I have completely neglected *systematic* errors in correcting galaxy shapes for PSF anisotropies. Eliminating these errors will certainly be much more difficult in ground-based images, both *LSST* and *WFHRI* type, because the PSF will have strong variation in both space and time. The density of point sources must be high enough to be able to track these variations to the desired accuracy.

5. Summary

The tools presented herein, while not particularly original or clever, permit one to optimize hardware and observing-protocol designs while accounting for effects that are typically ignored in aperture-photometry exposure-time estimates. Proper consideration of pixelization effects and cosmic-ray hits can easily change the expected S/N levels by a factor of 2, for example. With this machinery in hand, I have addressed a few issues of general interest, such as quantifying the effects of “oversized” pixels on photometric, astrometric, and lensing measurements, and showing that interlacing exposures in a 3×3 pattern will extract essentially all the useful information. The phase space of observations for which orbiting imagers are advantageous has been delineated as well. More importantly, the tools presented here are very general and flexible, and can be applied to a great variety of future design optimizations.

This work was supported by grant AST-9624592 from the National Science Foundation, and by DOE grant DE-FG-02-95-ER-40899. Thanks to Alex Kim and the members of the *SNAP*

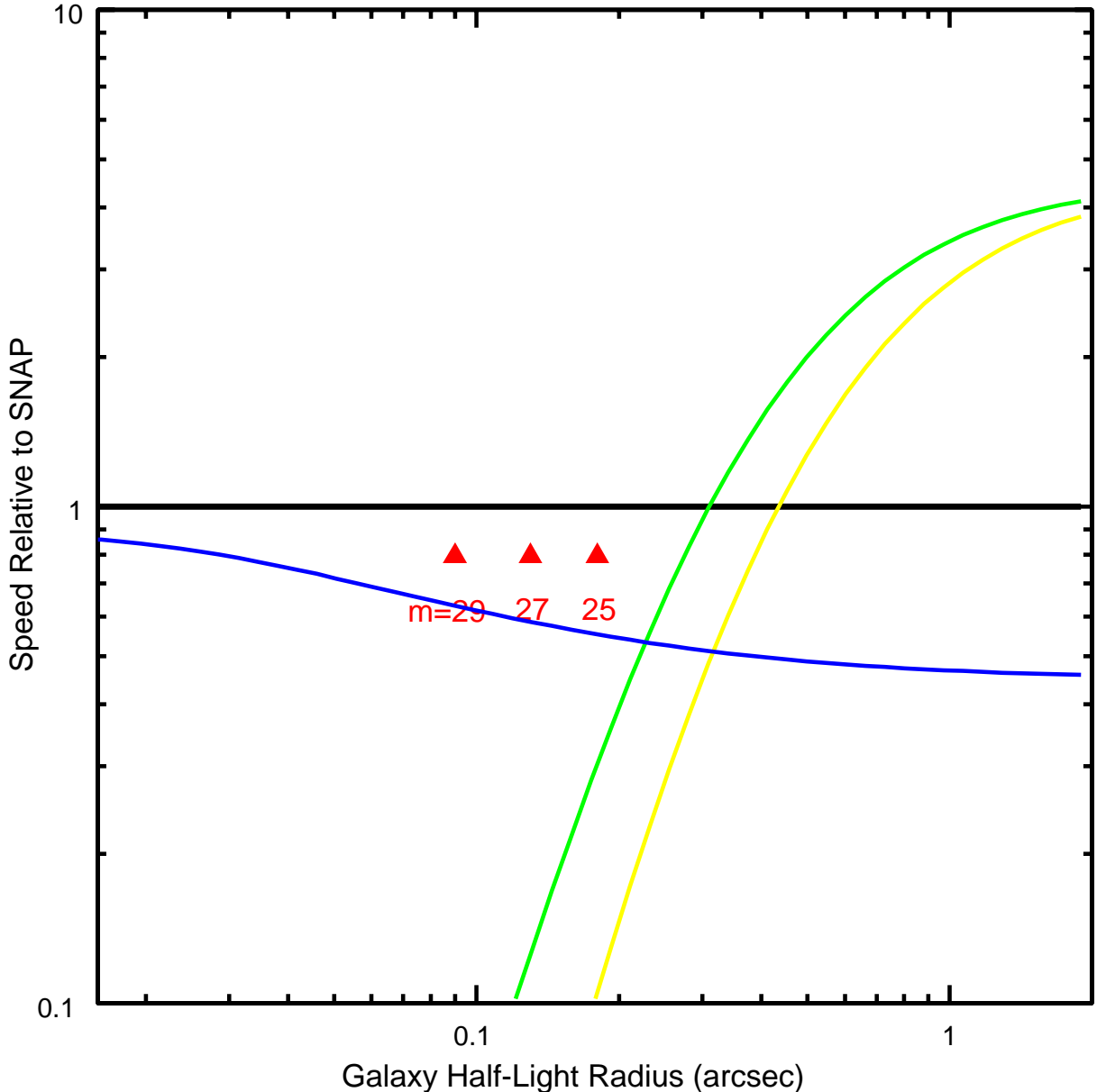


Fig. 8.— The survey speed for weak lensing observations (sky coverage divided by time to fixed ellipticity error at $m_{AB} = 27$) is given for *LSST* relative to *SNAP*. *SNAP* observations are assumed to be in *I* band, *LSST* in *R* band, and all observations are assumed to be background-limited with perfect systematic-error elimination. The green (yellow) curves assume Gaussian seeing with $0''.5$ ($0''.7$) FWHM. The typical sizes of faint galaxies in the HDF-S are marked. For such galaxies, *SNAP* has a modest to large speed advantage, whereas large galaxies are best done from the ground. The blue curve compares a *SNAP B*-band observation to the nominal *I*-band, assuming a typical galaxy color.

collaboration for having collected most of the relevant data.

REFERENCES

- Anderson, J., & King, I. R. 2000, PASP, 112, 1360
- Bracewell, R. N. 1978, *The Fourier Transfrom and Its Applications* (New York: McGraw-Hill)
- Gardner, J. P., & Satyapal, S. 2000, AJ, 119, 2589
- Groom, D. 2000, Proc SPIE, 4008, 634
- Hamuy, M. *et al.*, 1992, PASP, 104, 533
- Hamuy, M. *et al.*, 1994, PASP, 106, 566
- Hook, R. N., & Fruchter, A. S. 2000, *Astronomical Data Analysis Software & Systems IX*, Manset, Veillet, & Crabtree, eds., 521
- Kaiser, N., Tonry, J. L., & Luppino, G. A. 2000, PASP, 112, 768.
- Lauer, T. R. 1999a, PASP, 111, 227
- Lauer, T. R. 1999b, PASP, 111, 1434
- Leinert, C. *et al.*, 1997, A&AS, 127, 1
- Massey, P. *et al.*, 2000, <http://www.noao.edu/kpno/manuals/dim/dim.html>
- Roche, N., Ratnatunga, K., Griffiths, R. E., Im, M., & Naim, A. 1998, MNRAS, 293, 157
- Rauscher, B., Isaac, J., & Long, K. 2000, STScI-NGST-R-0003A
- Petro, L. & Stockman, H. 2000, AAS Mtg. 195, 138.01
- Stiavelli, M., Hanley, C., & Robberto, M. 1999, WFC3 Instrument Science Report 1999-01